Tricellulin Forms a Barrier to Macromolecules in Tricellular Tight Junctions without Affecting Ion Permeability

Susanne M. Krug,* Salah Amasheh,* Jan F. Richter,* Susanne Milatz,* Dorothee Günzel,* Julie K. Westphal,†‡ Otmar Huber,†‡ Jörg D. Schulzke,§ and Michael Fromm*

*Institute of Clinical Physiology, §Department of General Medicine, †Department of Laboratory Medicine and Pathobiochemistry, Charité, Freie Universität and Humboldt Universität, 12200 Berlin, Germany; and ‡Department of Biochemistry II, Friedrich-Schiller-Universität, 07743 Jena, Germany

Tricellulin is a tight junction protein localized in tricellular tight junctions (tTJs), the meeting points of three cells, but also in bicellular tight junctions (bTJs). To investigate its specific barrier functions in bTJs and tTJs, TRIC-a was expressed in low-level tricellulin–expressing cells, and MDCK II, either in all TJs or only in tTJs. When expressed in all TJs, tricellulin increased paracellular electrical resistance and decreased permeability to ions and larger solutes, which are associated with enhanced ultrastructural integrity of bTJs toward enhanced strand linearity. In tTJs in contrast, ultrastructure was unchanged and tricellulin minimized permeability to macromolecules but not to ions. This paradox is explained by properties of the tTJ central tube which is wide enough for passage of macromolecules, but too rare to contribute significantly to ion permeability. In conclusion, at low tricellulin expression the tTJ central tube forms a pathway for macromolecules. At higher expression, tricellulin forms a barrier in tTJs effective only for macromolecules and in bTJs for solutes of all sizes.

INTRODUCTION

Tight junctions are the main determinants of epithelial and endothelial barrier properties. A distinct composition of different transmembrane proteins including occludin and the family of claudins form this specific paracellular barrier. Barrier properties differ in electrical conductance and permeability for ionic and uncharged solutes depending on the local transport requirements (Furuse *et al.,* 1993, 1998; Van Itallie and Anderson, 2004; Schneeberger and Lynch, 2004).

The tight junctional (TJ) barrier is formed where strands of two neighboring cells contact laterally at paracellular spaces, forming a bicellular tight junction (bTJ; Tsukita *et al.,* 2001). At contact points of three cells, TJ strands form tricellular tight junctions (tTJs), which are structurally different. Here, electron microscopic examination of freeze-fracture replicas revealed that the network of bTJs extends basolaterally when converging at tricellular contacts, forming a vertically orientated triple pair strand structure with an ~10-nm "central tube" (Staehelin, 1973; Wade and Karnovsky, 1974; Walker *et al.,* 1994). This is in line with assumptions that the

Abbreviations used: bTJ, bicellular tight junction; TJ, tight junction; TRa-4, TRIC-a tricellular overexpression clone 4; TRa-8, TRIC-a bi- and tricellular overexpression clone 8; TRIC-a, human tricellulin isoform a; tTJ, tricellular tight junction.

tTJ is a site of elevated paracellular permeability (Staehelin *et al.,* 1969; Walker *et al.,* 1985; Ikenouchi *et al.,* 2005).

In the pioneering work of the late Shoichiro Tsukita it was shown that a basic element of tTJs is the distinct tetraspan transmembrane protein tricellulin (Ikenouchi *et al.,* 2005). As its name indicates, tricellulin is mainly localized in tricellular cell contacts, but it is present to a lesser extent also in bTJs.

Four isoforms of human tricellulin have been described so far (Riazuddin *et al.,* 2006): TRIC-a is the longest form (558 aa) and is meant in this as well as in other studies when simply termed "tricellulin." It contains seven exons and has a C-terminal ELL sequence with an overall identity of 32% (51% similarity) to occludin. Mutations of TRIC-a lead to nonsyndromic deafness, DFNB49 (Riazuddin *et al.,* 2006; Chishti *et al.,* 2008).

The isoform TRIC-a1 lacks the exon three and TRIC-b is a shorter isoform (458 aa) of tricellulin lacking the occludin-ELL. The occurrence of TRIC-b is hypothesized in basal cell layers of keratinocyte cultures (Schlüter *et al.,* 2007). TRIC-c (442 aa) is predicted to be a two-transmembrane domain protein with an alternatively spliced exon two.

At present, the characterization of tricellulin has been limited to the description of phenotypes and first results from a knockdown model. Suppression of TRIC-a expression by RNA interference resulted in compromised barrier function and disorganized tricellular and bicellular TJs, indicating that tricellulin is essential for barrier formation (Ikenouchi *et al.,* 2005). However, the authors regarded it premature to ultimately discuss the dysfunction of the epithelial barrier induced by suppressing tricellulin expression as only caused by the disorganization of tTJs, because tricellulin suppression appeared to affect the organization of not

only tTJs but also bTJs. The continuity of the TJ network was not maintained in the absence of tricellulin, and bTJs themselves appeared to be poorly developed (Ikenouchi *et al.*, 2005). From the observation that in occludin-deficient mice tricellulin was spread out in bTJ it was implied that occludin supports tTJ localization of tricellulin by excluding it from bTJ (Ikenouchi *et al.*, 2008).

By means of small interfering RNA techniques it seems difficult to study the barrier properties of tTJs and at the same time discriminating tricellular effects from those originating at the directly flanking bTJs. Here, we addressed exactly this point, to investigate the specific barrier mechanisms of human TRIC-a in bicellular and tricellular junctions in order to understand the functional importance of this protein. To this end, we followed a reverse strategy: instead of suppressing TRIC-a in a high-resistance cell line, we selected a low-resistance cell line with low intrinsic TRIC-a abundance and generated stable clones with either tricellular or tri- and bicellular overexpression of tricellulin. The stability of the clones allowed us to apply an ensemble of techniques including 1) molecular analyses, 2) ion selectivity measurements, 3) solute permeability measurements, 4) two-path impedance spectroscopy, 5) confocal fluorescence microscopy including 6) the newly developed technique of fluorescence live cell imaging of molecule passage, and 7) freeze-fracture electron microscopy.

Our studies revealed that tricellulin had different effects in bTJs and in tTJs. In bTJs it decreased permeabilities to ions and midsize to large solutes. In contrast, in tTJs tricellulin overexpression did not alter permeability to ions but strongly diminished the permeability to macromolecules of 4–10 kDa. A mechanistic explanation of this paradox is given by calculations of single tTJ central tube permeabilities and conductances and by observations of ultrastructural changes of bTJs but not tTJs. These findings indicate that at low tricellulin expression the central tube of tTJs forms a pathway for macromolecules.

MATERIALS AND METHODS

PCR Cloning of Human Tricellulin and Vector Construction

For cloning of the complete sequence of human tricellulin (TRIC-a), sense (5'-GCG GGT ACC CAA GCT TGC CGC CAT GTC AAA TGA TGG AAG ATC C-3') and antisense (5'-GCG GGT ACC AAG CTT TTA AGA ATA ACC TTG TAC ATC C-3') primers were synthesized according to the human tricellulin sequence (Ikenouchi *et al.*, 2005) and used for PCR (Metabion, Planegg-Martinsried, Germany) employing cDNA of the human colon cell line HT-29/B6 synthesized by reverse transcription. The resulting PCR product was ligated into pCR2.1-TOPO (Invitrogen, Karlsruhe, Germany), verified by cycle sequencing, and subsequently subcloned into the HindIII site of the eukaryotic expression vector pFLAG-CMV4. Next, the endogenous BamHI site in tricellulin was mutated without affecting the amino acid sequence and subsequently was amplified using oligonucleotides, 5'-GCG GGT ACC GGA TCC GCC GCC ATG TCA AAT GAT GGA AGA TCC-3' and 5'-GCG GGT ACC GGA TCC TTA AGA ATA ACC TTG TAC ATC-3'. After BamHI digestion, the PCR product was ligated into the BamHI site of p3x-FLAG-CMV10 (Sigma-Aldrich, Diesenhofen, Germany), and the sequence was confirmed by cycle sequencing.

Cell Culture and Transfections

MDCK II cells (Madin-Darby canine kidney cell subtype II, ATCC, Manassas, VA) were maintained in DMEM (DMEM) supplemented with 10% (vol/vol) fetal bovine serum (FBS), 100 U/ml penicillin, and 100 μg/ml streptomycin (Invitrogen). Cells were stably transfected using the Lipofectamine Plus protocol as described by the manufacturer (Invitrogen) with either p3xFLAG-pCMV10 as control or with p3xFLAG-pCMV10 containing the human tricellulin cDNA and selected in the presence of gentamicin G418. G418-resistant cell clones were screened for tricellulin overexpression by Western blotting and localization of tricellulin was analyzed using immunofluorescence microscopy, whereas the mock-transfected cells served as controls.

Electrophysiology

Cells were grown to confluence on porous polycarbonate microwell inserts (Millicell-HA, Millipore, Bedford, MA; 0.6-cm^2 area). Voltage and transepithelial resistance (R^t, $\Omega \cdot$ cm^2) were measured in Ussing chambers designed for cell filters (Kreusel *et al.*, 1991). Resistance of bathing solution and filter was measured before each experiment and subtracted. Ussing chambers and water-jacketed gas lifts were filled with 10 ml standard Ringer's solution (in mM: Na$^+$ 140; Cl$^-$ 149.8; K$^+$ 5.4; Ca^{2+} 1.2; Mg^{2+} 1; HEPES 10; and D(+)-glucose 10). pH was adjusted to 7.4 with NaOH. The solution was equilibrated with 100% O$_2$ at 37°C.

Single-ion permeabilities were determined from dilution or bi-ionic potentials and the Goldman-Hodgkin-Katz equation as reported previously (Amasheh *et al.*, 2002; Günzel *et al.*, 2009; Yu *et al.*; 2009). Briefly, NaCl dilution potentials were measured by switching one hemichamber to a solution containing a reduced concentration of NaCl and all other components identical to standard Ringer's. Osmolality was balanced by mannitol. For bi-ionic potentials, solution in one hemichamber was changed to one in which part of the NaCl was replaced isoosmotically by the respective cation-chloride or sodium-anion salt.

Two-Path Impedance Spectroscopy

Two-path impedance spectroscopy was performed similar to the method described by Reiter *et al.* (2006). Briefly, this method is based on a model describing the epithelial resistance, R^e, as a parallel circuit consisting of the transcellular resistance, R^{trans}, and the paracellular resistance, R^{para}. The subepithelial resistance, R^{sub}, is in series to R^e and, in cell cultures, is caused by the filter support. The apical and the basolateral membranes of the confluent cell layer are represented by resistors and capacitors in parallel (R^a, C^a, and R^b, C^b, respectively). R^a and R^b add up to R^{trans}. After application of AC (35 μA/cm^2, frequency range 1.3–65 kHz), changes in tissue voltage were detected by phase-sensitive amplifiers (402 frequency response analyzer, Beran Instruments, Gilching, Germany; 1286 electrochemical interface; Solartron Schlumberger, Farnborough, United Kingdom). Complex impedance values (Z$_{real}$, Z$_{imaginary}$) were calculated and plotted in a Nyquist diagram. This plot yields a semicircular arc as long as apical and basolateral membrane constants do not clearly differ (R^a C^a $\approx$ R^b C^B), which was true for the experiments of this study. R^{trans} and R^{para} were determined from experiments in which impedance spectra and fluxes of fluorescein as a paracellular marker substance were obtained before and after chelating extracellular Ca^{2+} with EGTA. This caused TJs to partly open and to increase fluorescein flux. It was ascertained in separate experiments that changes of fluorescein fluxes are inversely proportional to R^e changes (data not shown).

Flux Measurements of FITC-Dextran, [³H]PEG, and Fluorescein

All flux studies were performed in Ussing chambers under short-circuit conditions. Dextran flux was measured in 5 ml circulating Ringer's containing 10 mM unlabeled dextran on each side. After addition of 100 μl of 10 mM FITC-labeled dialyzed dextran (4-, 10-, or 20-kDa FITC-dextran; Sigma-Aldrich) to the apical bath, basolateral samples (300 μl) were collected at 0, 30, 60, 90, and 120 min. Tracer fluxes were determined from FITC-dextran samples, which were measured with a fluorometer at 520 nm (Spectramax Gemini, Molecular Devices, Ismaning, Germany). For fluorescein fluxes, Ussing chambers were filled with 10 ml Ringer's per side, 10 μl of fluorescein (100 mM) was added apically, and basolateral samples (300 μl) were replaced with fresh Ringer's 0, 10, 20, 30, and 40 min after addition. Fluxes of ³H-labeled PEG-400 and PEG-900 (Biotrend, Cologne, Germany) were measured in 10 ml of Ringer's containing 10 mM of unlabeled PEG. Apically 100 μl of the labeled PEG (10 mM) were added, a 100-μl sample was taken from the donor side, and 900 μl Ringer's and 4 ml of Ultima Gold high flashpoint liquid scintillation cocktail (Packard Bioscience) were added. Basolateral samples of 1 ml were collected at 0, 30, 60, 90, and 120 min after addition and replaced with fresh Ringer's. Samples were mixed with 4 ml of liquid scintillation cocktail and were subsequently analyzed with a Tri-Carb 2100TR Liquid Scintillation counter (Packard, Meriden , CT).

Horseradish peroxidase Flux Measurements

Cells grown on filter supports were mounted in Ussing chambers containing 5 ml circulating Ringer's solution. After addition of 100 μl of 20 μM horseradish peroxidase (HRP) solution (HRP type VI, Sigma-Aldrich) on the apical side, basolateral samples of 300 μl were replaced with fresh Ringer's at -10, 10, 40, 70, 100, and 130 min after addition of HRP. Samples were analyzed using a fluorogenic peroxidase substrate (QuantaBlu, Pierce, Bonn, Germany) for reaction and measuring in a fluorometer (Spectramax Gemini) using wavelengths of 325 nm (excitation) and 420 nm (emission).

Western Blotting

Cells were washed with ice-cold PBS, scraped from the permeable supports, and incubated on ice in lysis buffer containing 10 mM Tris-Cl (pH 7.5), 150 mM NaCl, 0.5% (vol/vol) Triton X-100, 0.1% (wt/vol) SDS, and protease inhibitors (Complete, Roche, Mannheim, Germany). Protein was obtained in

Figure 1. Endogenous expression of TRIC-a in epithelial cell lines and overexpression of human 3xFLAG-TRIC-a in MDCK II cells. (A) Membrane protein fractions of the human TRIC-a (64 kDa) in the human intestinal cell lines HT-29/B6, CaCo-2, and T84, the canine tricellulin (62 kDa) in MDCK II and, for comparison, 3×FLAG-TRIC-a (72 kDa) in overexpression clone TRa-4. At a height of ~80 kDa a distinct additional band was detected, which was assumed to be a yet undefined isoform of tricellulin that already had been observed, but not further analyzed, by Riazuddin *et al.* (2006). (B) Localization of endogenous tricellulin (green) and the TJ marker occludin (red) in MDCK II cells by immunofluorescence confocal microscopy. These cells exhibit low endogenous tricellulin, which is colocalized with occludin preferably within tTJs (yellow). Bar, 20 μm. (C) Using anti-FLAG antibody, Western blots of TRIC-a–overexpressing clones in comparison with vector-transfected controls and untransfected cells showed that in both TRa clones 3×FLAG-TRIC-a is expressed in bands of the predicted size of 72 kDa, whereas neither vector controls nor untransfected MDCK II gave signals at the molecular mass of TRIC-a. Employing a polyclonal anti-tricellulin antibody, endogenous tricellulin was detectable in all four cell types, whereas additional 3×FLAG-TRIC-a was detectable in both TRa clones.
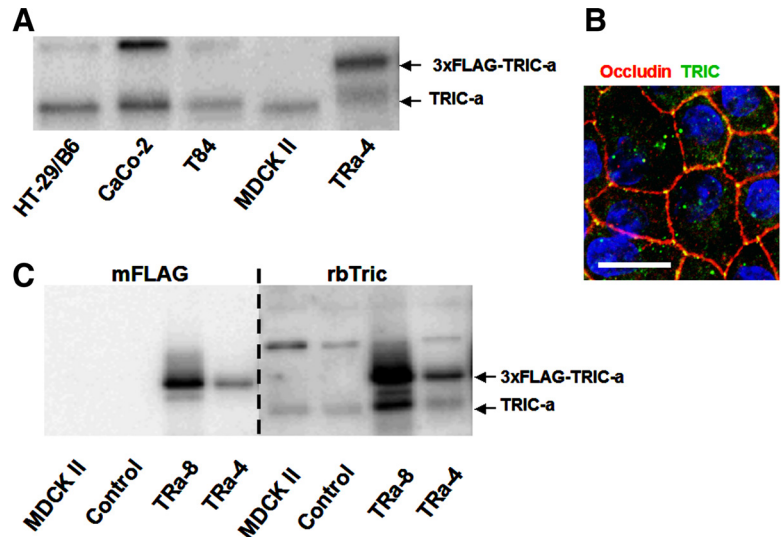
the supernatant after a centrifugation at 15.000 × *g* (15 min, 4°C). Concentration of protein content was determined using BCA Protein assay reagent (Pierce, Bonn, Germany) and quantified with a plate reader (Tecan, Hillsborough, NC). Tenn micrograms of the protein samples was mixed with SDS-sample buffer (Laemmli), electrophoresed on an SDS-polyacrylamide gel, and transferred to a PVDF membrane (Perkin Elmer-Cetus, Norwalk, CT). Proteins were detected by immunoblotting employing primary antibodies against occludin and claudin-1, -2, -3, and -4 (Invitrogen), FLAG-M2 (Sigma-Aldrich), and an antibody against tricellulin using purified His6-tagged C-terminal tail of human TRIC-a as an antigen. His6-tagged TRIC C-term was expressed in *Escherichia coli* BL-21-RE4 and purified on Ni-NTA agarose under denaturing conditions (Qiagen, Hilden, Germany). Subsequently the eluate was loaded onto a preparative SDS-polyacrylamide gel and stained with KCl. The His6-tagged TRIC C-term band was cut out and crushed into small pieces, and the protein was eluted over night. This highly pure protein was used for immunization of rabbits and a guinea pig (Pineda-Antikörper-Service, Berlin, Germany). After washing steps in PBST, membranes were incubated with secondary anti-mouse or anti-rabbit antibodies. For chemiluminescence detection membranes were washed and incubated with Lumilight (Roche). Specific signals were quantified by luminescence imaging (LAS-1000, Fujifilm, Tokyo, Japan) and quantification software (AIDA, Raytest, Straubenhardt, Germany).

TUNEL Staining

Cells were fixed in formaldehyde. After embedding in paraffin, DNA was stained with a TUNEL assay (TdT-mediated X-dUTP nick end labeling; Roche) and blunt ends of double-stranded DNA exposed by strand breaks were visualized by means of enzymatic labeling of the free 3′-OH termini with fluorescein-dUTP.

Immunofluorescence Microscopy

Immunofluorescence microscopical analyzes were performed as reported by Florian *et al.* (2003). Briefly, cells were grown on 18 × 18-mm coverslips to confluence, rinsed with PBS, fixed with methanol, and permeabilized with PBS containing 0.5% (vol/vol) Triton X-100. Antibodies were diluted in blocking solution: mouse anti-FLAG-M2 (Sigma-Aldrich) 1:500; rabbit anti-occludin (Invitrogen) 1:200 and guinea pig anti-tricellulin 1:1000; Alexa Fluor 488 goat anti-guinea pig, 1:2000, Alexa Fluor 488 goat anti-mouse and Alexa Fluor 594 goat anti-rabbit, 1:500 (Molecular Probes, Hamburg, Germany; MoBiTec). Immunofluorescence images were obtained with a confocal laser scanning microscope (LSM 510 Meta, Carl Zeiss, Jena, Germany), using excitation wavelengths of 543 and 488 nm.

Fluorescence Live-Cell Imaging of Molecule Passage

Cells were seeded inversely on Transwell permeable supports (Corning, Corning, NY) and grown to confluence. Confocal imaging was carried out in a temperature-controlled chamber, whereby cells were apically covered with 5% (wt/vol) low-melt agarose (Invitrogen) to facilitate accumulation of passed-through solutes. Labeled dextrans (TMR-dextran, 3 kDa; OG-dextran, 70 kDa, Invitrogen; 4 μM each) were added basolaterally, and passage was visualized over time using appropriate laser lines (see Supplemental Material 1 for further information).

Freeze-Fracture Electron Microscopy

Freeze-fracture electron microscopy was performed as previously described (Zeissig *et al.*, 2007). Briefly, cells grown on permeable supports were fixed with phosphate-buffered glutaraldehyde (2%). Preparations were incubated in 10% (vol/vol) and then in 30% (vol/vol) glycerol and finally were frozen in liquid nitrogen-cooled Freon 22. Cells were fractured at −100°C and shadowed with platinum and carbon in a vacuum evaporator (Denton Vacuum, Cherry Hill, NJ; DV-502). Replicas were bleached with sodium hypochloride, picked up on grids (Ted Pella, Irvine, CA), and analyzed with a video-equipped Zeiss 902 electron microscope (Carl Zeiss AG; Olympus, Melville, NY; iTEM Veleta).

Morphometrical analysis was performed at a final magnification of 51,000×. Vertical grid lines were drawn at 200-nm intervals perpendicular to the most apical TJ strand (Stevenson *et al.*, 1988). The number of strands horizontally oriented within the main TJ meshwork was counted at intersections with grid lines. The distance between the most apical and contraapical strand was measured as the meshwork depth. Strand discontinuities within the main compact TJ meshwork of >20 nm were defined as "breaks," and their number is given per μm length of horizontally oriented strands. Strand formation was noted as "particle type" or "continuous type."

Statistical Analysis

Data are expressed as mean values ± SEM, indicating n as the number of single measurements. Statistical analysis was performed using Student's *t* test with Bonferroni-Holm correction for multiple testing. $p < 0.05$ was considered significant (* $p < 0.05$, ** $p < 0.01$, *** $p < 0.001$).

RESULTS

Expression of Tricellulin in tTJs versus bTJs

Endogenous tricellulin (TRIC-a) expression was analyzed in several epithelial cell lines, including the intestinal cell lines HT-29/B6, Caco-2, and T84 and the kidney tubule cell lines MDCK II (Figure 1A), MDCK I and M-1, and human keratinocytes HaCaT (data not shown). In all cell lines endogenous TRIC-a was detectable, and for overexpression studies we selected the low-resistance cell line MDCK II, because of the lowest endogenous tricellulin expression. Despite this low expression a preferred junctional localization within tTJs was apparent (Figure 1B). cDNA of human TRIC-a, which was tagged with an N-terminal 3×FLAG tag, was stably transfected into MDCK II cells, and the tricellulin expression in the resulting clones was analyzed by Western blotting, employing an anti-FLAG antibody and a polyclonal antibody raised against the C-terminus of human tricellulin, respectively (Figure 1C).
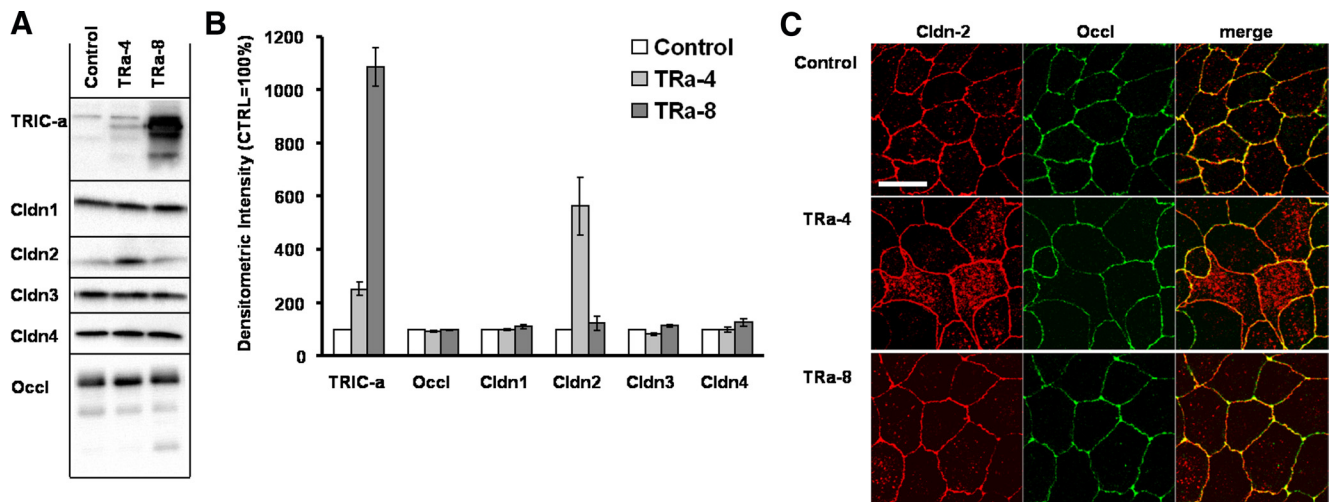
Figure 2. Expression of occludin, claudin-1, -2, -3, -4, and tricellulin (A and B) and localization of claudin-2 (C) in 3×FLAG-tricellulin-transfected cells. (A) Tricellulin, occludin, and claudin-1, -2, -3, and -4 were detected by Western blotting in vector-transfected controls and two representative TRa-a–overexpressing clones. (B) 3×FLAG-TRIC-a is strongly overexpressed in clone TRa-8 and only moderately in clone TRa-4. Expression of occludin, claudin-1, -3, and -4 remained constant, whereas in TRa-4 expression of claudin-2 was increased as shown by densitometric analysis (n = 4). (C) Localization of claudin-2 (red) and the TJ marker occludin (green) in mock-, TRa-4–, and TRa-8–transfected cells by confocal microscopy. In TRa-4 cells additional claudin-2 was predominantly localized in intracellular compartments, whereas membrane staining was not changed. TRa-8 cells showed similar staining to the vector control. Bar, 20 μm.

From several clones that differed in TRIC-a expression levels, two clones representing different localization of overexpressed tricellulin, TRa-4 and -8, were chosen for detailed characterization, whereas several remaining clones were used for confirmation of the key experiments (Supplemental Material 3). These remaining clones gave results nearly identical to those obtained with TRa-4 and -8. In clone TRa-4 tricellulin expression was moderate (252 ± 26% of vector control, n = 4) and in a range comparable to that of the human intestinal epithelial cell lines Caco-2 and HT-29/B6 (Figure 1A). Because these cell lines are well-established models of human colon, the expression rate of tricellulin in TRa-4 may resemble the conditions in the colon.

In contrast, clone Tra-8 was characterized by strong overexpression of TRIC-a compared with the vector-transfected control (1086 ± 72%, n = 4; Tra-4: 252 ± 26%, n = 4; Figure 2, A and B). Expression analysis of other TJ proteins employing the respective antibodies revealed no significant changes in the expression and localization of occludin, claudin-1, -3, and -4 (Figure 2, A and B), except claudin-2, which was increased in TRa-4 cells as detected by Western blotting (562 ± 110% in comparison with vector-transfected controls; n = 4). To check whether or not the additional claudin-2 was localized within the TJ, immunostaining of claudin-2 (red) and the TJ marker occludin (green) was performed and revealed that the additional claudin-2 was predominantly localized in intracellular compartments and thus did not contribute to paracellular barrier mechanisms (Figure 2C).

Localization of the 3×FLAG-TRIC-a in TJs was examined by confocal immunofluorescence microscopy, using polyclonal anti-tricellulin and anti-occludin antibodies, respectively. Z scans were performed (Figure 3A), and two-dimensional intensity profile plots were generated (Figure 3B).

In stainings of vector-transfected controls, specific signals were visible at tricellular contacts, representing endogenous canine tricellulin. Also in the bTJ weak signals for tricellulin were detectable, colocalizing with occludin (Figure 3B, left). Clone TRa-4 cells showed a weak expression of tricellulin in bTJs at a level comparable to control cells, but exhibited clearly increased tricellulin staining at tTJs in colocalization with occludin (Figure 3B, middle). Clone TRa-8, which was characterized by strong overexpression of TRIC-a, showed tricellulin expression at tTJs that was comparable to that of clone TRa-4, but the signals, colocalizing with occludin, were strongly extended to bTJs (Figure 3B, right), and thus this clone was used to describe the effect of tricellulin in bTJs.

Paracellular Resistance and Ion Permeabilities Are Only Altered upon Bicellular Expression of Tricellulin

Two-path impedance spectroscopy was applied to obtain paracellular resistance (R^{para}), reflecting the resistance of the TJ, and transcellular resistance (R^{trans}), reflecting the apical and basolateral cell membrane. Thus, epithelial resistance (R^e) represents the contribution of both resistances in parallel, R^{para} and R^{trans} (Figure 4). In controls, R^{trans} (69 ± 19 $\Omega \cdot cm^2$) exceeded R^{para} (44 ± 11 $\Omega \cdot cm^2$), indicative of a leaky epithelium with an R^e of 21 ± 3 $\Omega \cdot cm^2$ (n = 6).

In TRa-4 cells, none of these resistances were significantly altered in comparison with controls (R^{para}, 45 ± 15 $\Omega \cdot cm^2$; R^{trans}, 51 ± 9 $\Omega \cdot cm^2$; R^e, 25 ± 4 $\Omega \cdot cm^2$; n = 7) indicating that TRIC-a overexpression solely in tTJ had no effect on ion permeation.

In contrast, R^{para} was increased 14-fold in TRa-8 (612 ± 141 $\Omega \cdot cm^2$, ** p < 0.01) compared with controls, whereas R^{trans} was again unaltered (83 ± 9 $\Omega \cdot cm^2$) versus control or TRa-4 cells, respectively. This resulted in a threefold rise of epithelial resistance (R^e 72 ± 9 $\Omega \cdot cm^2$; ** p < 0.01, n = 6) and indicated that pronounced overexpression of TRIC-a in bTJs in addition to tTJs can decrease ion permeability, causing formation of an epithelium of pronounced tightness (Figure 4).

Tricellulin-induced Barrier Exhibits No Charge Preference and No Striking Change in Ion Selectivity

Changes in resistance were further analyzed by transepithelial permeability assays with different ions using dilution and bi-ionic potential measurements (Figure 5). Comparing
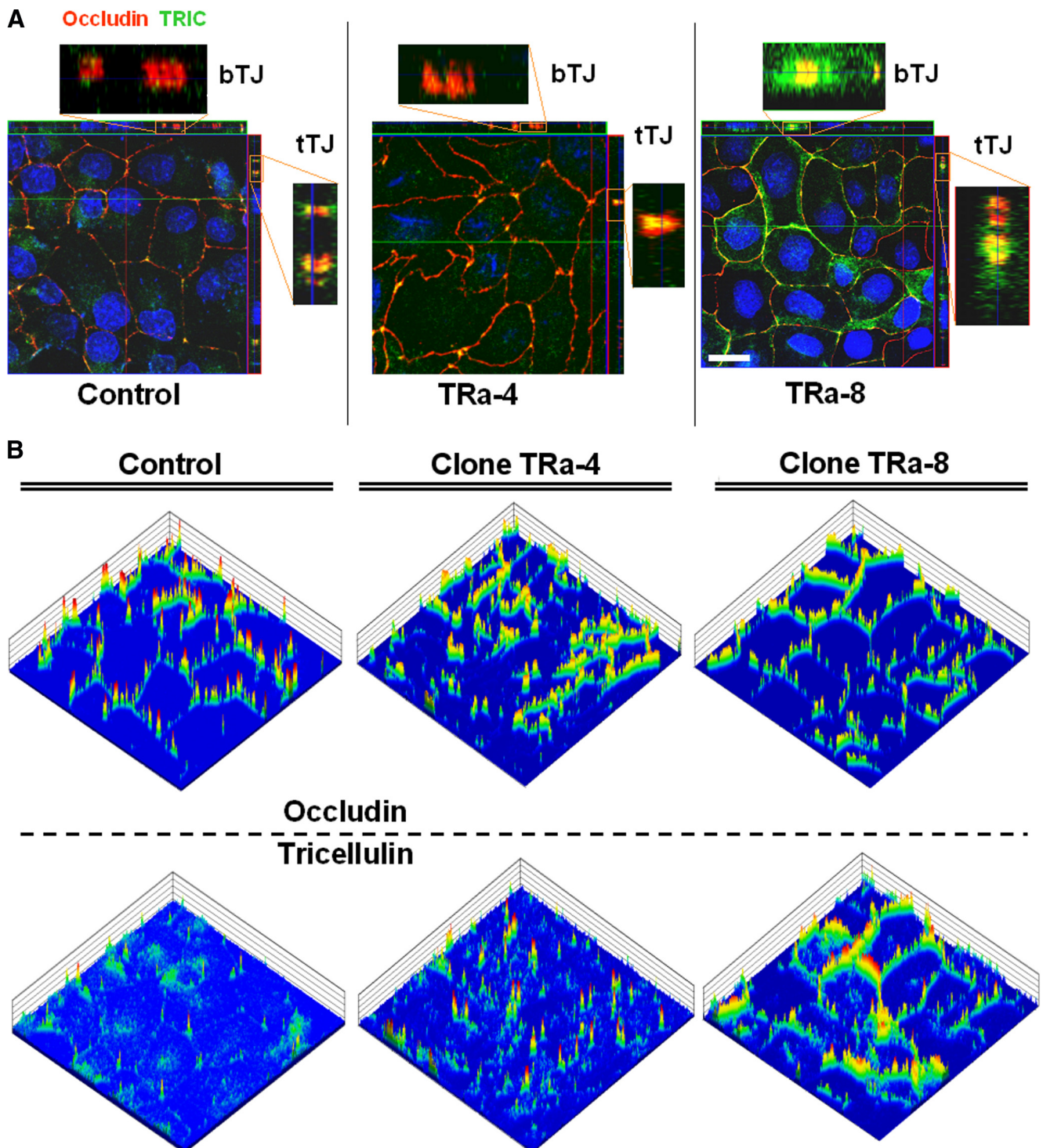
Figure 3. Localization of tricellulin and occludin in TRa-4 and -8 cells by immunofluorescence microscopy. (A) Z-scans of vector controls showed localization of endogenous tricellulin (green) mainly at tricellular contacts in colocalization (yellow) with occludin (red). In TRa-4 cells similar localization was detectable with additional weak intracellular signals. In contrast, TRa-8 cells revealed strong signals for tricellular as well as bicellular TJ, still colocalizing with occludin. Bar, 20 μm. Because record settings were optimized to vector-transfected controls, which showed only weak endogenous expression of tricellulin, also intracellular signals became visible. (B) Intensity plot analysis of the immunofluorescence signals revealed a consistent cell–cell contact localization of occludin in all three clones. Tricellulin preferentially localizes in tricellular contacts; however, weak signals were also detectable in bTJs in vector-transfected cells. Enhanced staining in tTJs was detectable in TRa-4 cells, indicating that transfected TRIC-a is predominantly localized there. TRa-8 cells showed high signal intensities also in bTJs (area: 115 $\times$ 115 μm).

controls with TRa-4 cells showed no significant change in permeability for Na$^+$ (control, 43.3 $\pm$ 3.3 $\times$ 10^{-6} cm/s; TRa-4, 39.0 $\pm$ 0.4 $\times$ 10^{-6} cm/s; n = 6) or for Cl$^-$ (control, 13.8 $\pm$ 2.1 $\times$ 10^{-6} cm/s; TRa-4, 13.1 $\pm$ 1.7 $\times$ 10^{-6} cm/s; n =
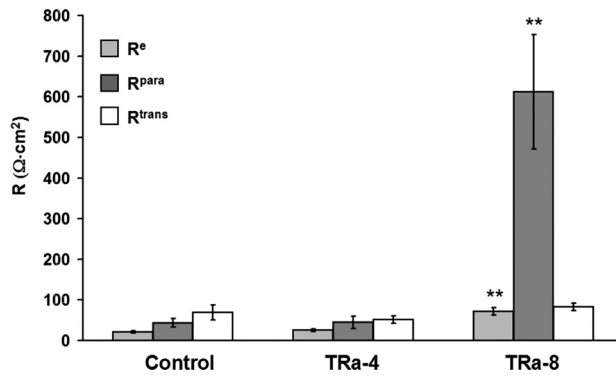
Figure 4. Two-path impedance spectroscopy. Tricellular overexpression of TRIC-a in TRa-4 cells did not change epithelial resistance (R^e) in comparison to controls, whereas bicellular overexpression of TRIC-a in TRa-8 cells induced a threefold increase of R^e (** $p < 0.01$; $n = 6, 7$, and 6, respectively). This increase was caused by 14-fold rise of paracellular resistance (R^{para}, ** $p < 0.01$), which is determined by the ion permeability of the TJ. Transcellular resistance (R^{trans}) was not significantly changed.

6). In contrast, in TRa-8 cells both permeabilities were reduced, i.e., for Na^+ to $12.7 \pm 0.8 \times 10^{-6}$ cm/s and for Cl^- to $4.2 \pm 0.3 \times 10^{-6}$ cm/s (both $n = 5$, *** $p < 0.001$; Figure 5A).

The ratio P_{Na}/P_{Cl} was constant in all groups (control, 3.14 ± 0.28; TRa-4, 3.00 ± 0.39; TRa-8, 3.03 ± 0.03; $n = 5–6$, n.s.), indicating that charge preference was not affected by TRIC-a (Figure 5B). Especially for the TRa-4 clone this underlines that the change in claudin-2 expression had no functional relevance, because a change in Na^+ permeability would be expected after elevated expression of properly located claudin-2, because claudin-2 is known to form specific paracellular channels for small cations (Furuse *et al.*, 2001; Amasheh *et al.*, 2002).

The results in P_{Na} and P_{Cl}, and thus also in P_{Na}/P_{Cl}, were fully confirmed in two additional clones of each group (Supplemental Material 3, Supplemental Figure S2).

To characterize TRIC-a–induced changes in ion permeabilities in more detail, permeability sequences of monovalent cations and anions (Eisenman sequences) as well as divalent cations (Sherry sequences) were analyzed, describing the interaction between permeating ions and a conducting pore. Because no changes in ion permeability in clone TRa-4 were observed, we focused on the bTJ overexpression of tricellulin in TRa-8.

The Eisenman sequence for monovalent cations was determined in controls as being $Na^+ \geq K^+ > Li^+ > Rb^+ > Cs^+$

(Eisenman sequence IX), whereas overexpression of TRIC-a in bTJs (TRa-8) resulted in a slight shift to $Na^+ > Li^+ > K^+ > Rb^+ > Cs^+$ (Eisenman sequence X) and an average fourfold reduction in absolute permeabilities (Figure 6A).

The sequence for divalent cations was found to be $Ca^{2+} > Ba^{2+} > Sr^{2+} > Mg^{2+}$ in controls (Sherry sequence III) and $Ca^{2+} > Mg^{2+} > Ba^{2+} > Sr^{2+}$ for TRa-8 cells (Sherry sequence V), with an average permeability decrease of 50% (Figure 6B).

The sequence for monovalent anions could not be univocally determined because F^- proved to be toxic to the cells and had therefore to be omitted. Taking this into account, our measurements also revealed an only minor shift from $Cl^- > Br^- > I^-$ in controls (Eisenman IV–VII) to $Br^- > Cl^- > I^-$ for TRa-8 (Eisenman III), again with an average permeability decrease by half (Figure 6C).

Size-dependent Permeabilities Differ between Bicellular and Tricellular Expression of Tricellulin

Fluxes of paracellular markers of molecular weights between 332 Da and 20 kDa were measured to determine the limiting size for permeability. Permeability for fluorescein (332 Da), a divalent midsized anion, was determined as $4.80 \pm 1.21 \times 10^{-6}$ cm/s ($n = 6$) in controls. Overexpression of TRIC-a localized at tTJs in TRa-4 cells did not affect permeability for fluorescein ($4.58 \pm 1.03 \times 10^{-6}$ cm/s, $n = 9$). However, in TRa-8 cells with bicellular localization of TRIC-a, a substantial decrease in permeability to $1.85 \pm 0.21 \times 10^{-6}$ cm/s was detectable ($n = 10$, * $p < 0.05$, Figure 7A). Fluxes of an uncharged molecule of similar size, PEG-400 (400 Da), gave similar results (controls, $5.11 \pm 0.29 \times 10^{-6}$ cm/s, $n = 9$; TRa-4, $5.63 \pm 0.33 \times 10^{-6}$ cm/s, $n = 12$, n.s. vs. control; TRa-8, $3.92 \pm 0.12 \times 10^{-6}$ cm/s, $n = 11$, ** $p < 0.01$, Figure 7B), indicating that for midsized molecules changes in permeability were independent of charge.

A marker molecule size of 900 Da (PEG 900), revealed a reduction in permeability also in TRa-4 (controls, $4.78 \pm 0.48 \times 10^{-6}$ cm/s, $n = 4$; TRa-4, $3.42 \pm 0.19 \times 10^{-6}$ cm/s; $n = 6$, * $p < 0.05$), whereas for TRa-8 cells the permeability of PEG-900 was reduced to $2.76 \pm 0.28 \times 10^{-6}$ cm/s ($n = 7$; ** $p < 0.01$, Figure 7C).

FITC-4K-dextran, a macromolecule of 4 kDa, showed a 10-fold decrease in permeability compared with PEG 900 in control cells ($0.48 \pm 0.10 \times 10^{-6}$ cm/s, $n = 6$). In TRa-4 cells the permeability for FITC-4K-dextran was reduced dramatically to 15% of controls ($0.07 \pm 0.02 \times 10^{-6}$ cm/s, $n = 6$, ** $p < 0.01$) and was lowered even more in TRa-8 cells ($0.02 \pm 0.03 \times 10^{-6}$ cm/s, $n = 8$; *** $p < 0.001$, Figure 7D). The permeability for the 10-kDa macromolecule, FITC-10K-
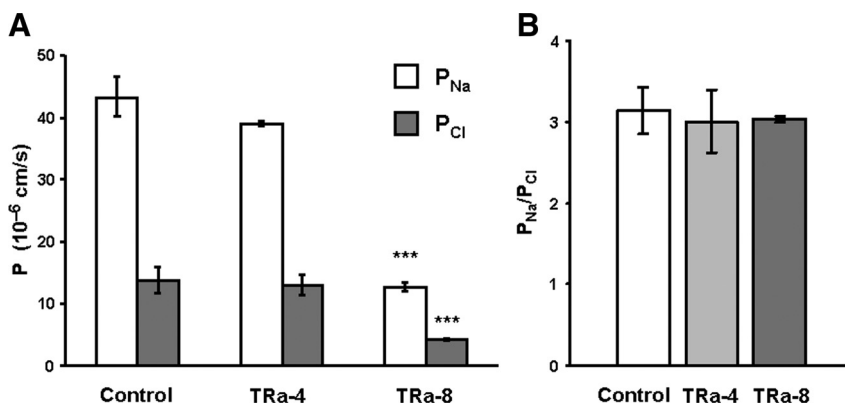

Figure 5. Dilution potential measurements for Na^+ and Cl^-. (A) Permeability for Na^+ and Cl^-. Dilution potential measurements revealed no difference in permeability for Na^+ (white bars) and Cl^- (dark gray bars) for vector controls and TRa-4 cells ($n = 6, 6$), whereas TRa-8 cells showed reduced permeabilities for both ions (P_{Na}: *** $p < 0.001$; P_{Cl}: *** $p < 0.001$; $n = 5$). (B) Changes in permeability for P_{Na} and P_{Cl} in TRa-8 cells did not affect the P_{Na}/P_{Cl} ratio, demonstrating no altered charge preference after TRIC-a overexpression ($n = 6, 6$, and 5, respectively).
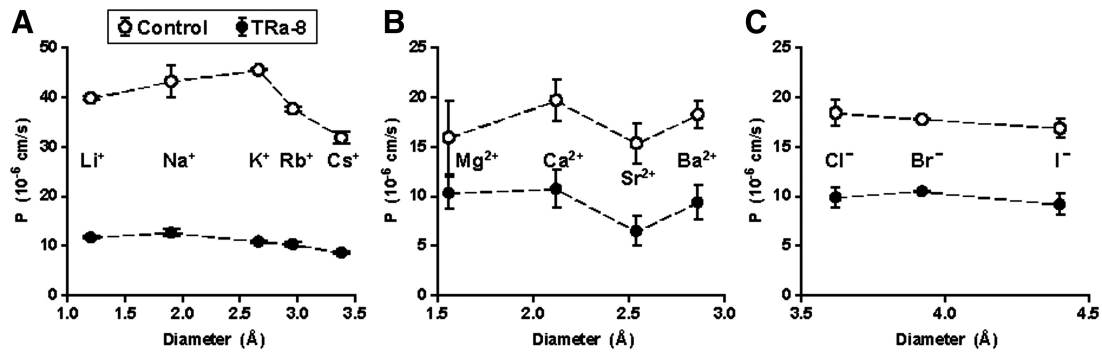
Figure 6. Permeabilities for monovalent cations, anions, and divalent cations, comparing vector controls (○) and TRa-8 cells (●). (A) Monovalent cations. Permeabilities for monovalent cations resulted in Eisenman sequence IX for the vector control and X for TRa-8 cells, indicating a change to a marginally stronger interaction with unhydrated ions. In general, permeabilities were reduced for all monovalent cations (P_{Li}: n = 4 and 7, *** p < 0.001; P_K: n = 6 and 9, *** p < 0.001; P_{Na}: n = 6 and 5, *** p < 0.001; P_{Rb}: n = 5 and 8, *** p < 0.001; P_{Cs}: n = 6 and 15, respectively, *** p < 0.001). (B) Divalent cations. Permeabilities for divalent cations resulted in Sherry sequence III for the mock-transfected and V for TRa-8 cells, showing again a change to a marginally stronger interaction with unhydrated ions. In general, permeabilities were reduced for all divalent cations, except Mg^{2+} (P_{Mg}: n = 9 each; P_{Ca}: 7 each, ** p < 0.01; P_{Sr}: n = 5 each, ** p < 0.01; P_{Ba}: n = 8 and 7, respectively, ** p < 0.01). (C) Monovalent anions. Permeabilities for monovalent anions resulted in Eisenman sequence IV-VII for the vector-transfected cells and III for TRa-8 cells, here suggesting a change to a slightly stronger interaction with hydrated ions. In general, permeabilities were reduced for all measured anions.(P_{Cl}: n = 29 and 28, *** p < 0.001; P_{Br}: n = 10 and 8, *** p < 0.001; P_I: n = 5 each, *** p < 0.001).

dextran, was $0.13 \pm 0.03 \times 10^{-6}$ cm/s (n = 5) in control cells. Consistently, in TRa-4 cells permeability was greatly reduced to 23% of controls ($0.03 \pm 0.01 \times 10^{-6}$ cm/s, n = 5 ** p < 0.01). Moreover, in TRa-8 cells permeability for the 10-kDa dextran was undetectable ($0.00 \pm 0.01 \times 10^{-6}$ cm/s, n = 5; ** p < 0.01, Figure 7E). This indicates that TRIC-a overexpression in tTJ (TRa-4 cells) affected permeation of 4- and 10-kDa macromolecules, but not of solutes smaller than 400 Da. Because of the strong decrease of macromolecule permeability in TRa-4 cells, it should be noted that also in these experiments routinely monitored transepithelial resistance did not differ from that of controls (data not shown).

The results for fluorescein and 4K-dextran were fully confirmed in several additional clones of each group (Supplemental Material 3, Supplemental Figure S3).

Permeability for 20-kDa FITC-dextran was almost negligible and similar in controls and in both TRIC-a–transfected clones (control, $6.1 \pm 1.3 \times 10^{-9}$ cm/s, n = 6; TRa-4, $3.0 \pm 1.1 \times 10^{-9}$ cm/s, n = 5; TRa-8, $3.8 \pm 0.6 \times 10^{-9}$ cm/s, n = 6, Figure 7F). This indicates an upper limit for macromolecule passage across the TJ of MDCK II cells on the order of 20 kDa.

Transcytosis or Apoptosis Are Not Involved in Permeability Changes

Transcytotic passage of macromolecules was determined from HRP fluxes. Permeabilities for HRP (approximately 44 kDa) were smaller by several orders of magnitude than those for all other molecules studied above and were not significantly different in controls and both TRIC-a clones (controls, $2.35 \pm 0.47 \times 10^{-12}$ cm/s, n = 4; TRa-4, $1.79 \pm 0.67 \times 10^{-12}$ cm/s, n = 5; TRa-8, $1.92 \pm 0.49 \times 10^{-12}$ cm/s, n = 4; Figure 7G). It can therefore be excluded that the permeabilities measured in this study were affected by cellular passage via transcytosis.

To measure epithelial apoptosis which might induce macromolecule permeability, histology on TUNEL-stained monolayers was performed. The fraction of apoptotic cells was $0.83 \pm 0.34\%$ in controls, $0.87 \pm 0.35\%$ in TRa-4 cells, and $0.67 \pm 0.27\%$ in TRa-8 cells (n = 6, n.s., Figure 7H). Thus, a change in apoptotic rate also can be excluded as a cause for altered macromolecule passage after TRIC-a overexpression.

Visualization of Macromolecular Passage across tTJs and bTJs

Local macromolecule passage was directly visualized by fluorescence live-cell imaging. Rapid dispersion of labeled dextrans after passage from the basolateral to the apical side was prevented by placing an agarose gel on top of the cell monolayer. Simultaneous basolateral application of a 3-(red) and a 70-kDa (green) dextran confirmed that the 70-kDa dextran was not able to pass the monolayer, whereas signals for the 3-kDa dextran increased with time above the apical surface of monolayers (Figure 8, B and C). The 70-kDa dextran, therefore, served as control for monolayer integrity over time.

In vector-transfected controls the 3-kDa signals increased over time above cell–cell junctions and mixed with signals of neighboring cells (Supplemental Material 1, Movie). From corresponding XZ scans the localization of 3-kDa dextran passage was assigned to both, bTJs and tTJs (Figure 8A). At present, these measurements are close to the resolution limits of this new technique. An exemplary image from the movie file (taken 23 min after marker addition) shows local 3-kDa dextran signals above two neighboring tTJs and to a lesser degree above bTJs. This indicates a paracellular passage of macromolecules at tTJs and also at bTJs under conditions where permeability is not reduced by additional tricellulin (Figure 8D).

Bicellular Junctions Are More Continuous at the Ultrastructural Level after TRIC-a Overexpression

To obtain insight as to how tricellulin affects the TJ and increases its barrier properties, the ultrastructure of both, bTJs and tTJs were analyzed by freeze-fracture electron microscopy (Figure 9).

Comparison of the bTJs (Figure 9, A–C) of controls, TRa-4, and TRa-8 showed no alteration in the horizontally oriented strands arranged perpendicular to the paracellular diffusion pathway, whether analyzed as frequency distribution or at absolute numbers (Figure 10, A and B). Neither the numbers of strands (control, 4.36 ± 0.24, n = 11; TRa-4, 4.61 ± 0.31, n = 11; TRa-8, 4.81 ± 0.30, n = 10, n.s.; Figure 10B) nor the meshwork depth was changed in any clone (control, $246 \pm$
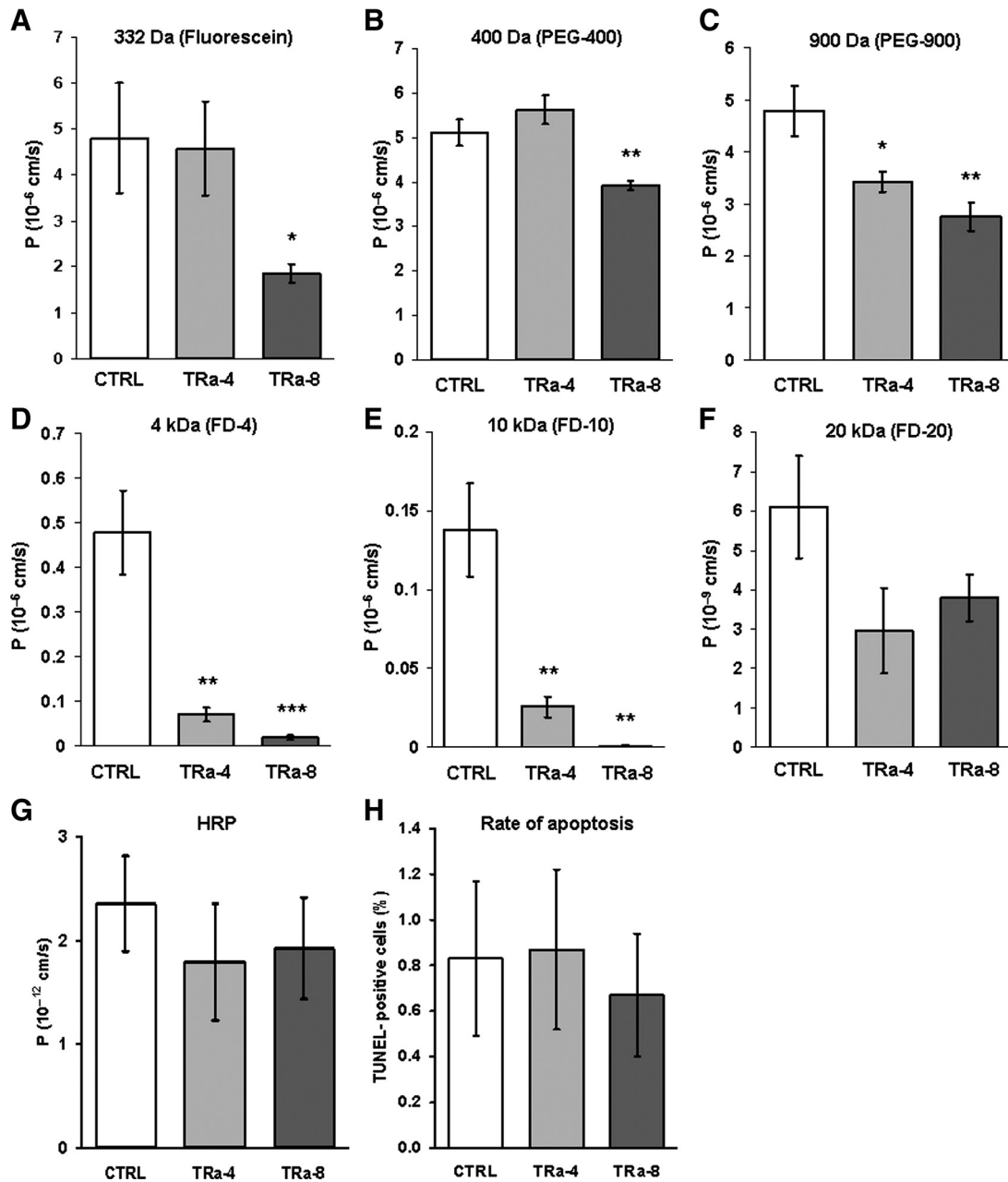
Figure 7. Permeabilities of paracellular, macromolecular, and transcytotic flux markers. Permeability measurements of paracellular markers revealed a passage of macromolecules in a range from ~400–900 Da up to 10–20 kDa in tricellular overexpression clones, whereas bicellular overexpression clones showed permeation already for smaller molecules. (A) Fluorescein (332 Da) was used as a twice negative–charged paracellular flux marker. In comparison with the vector-transfected cells permeabilities were decreased in TRa-8 cells and remained unchanged in TRa-4 cells (n = 6, 9, and 10; ** p < 0.01). (B) Permeability for PEG-400 remained similar in mock-transfected and TRa-4 cells, whereas it was decreased in TRa-8 cells (n = 9, 12, and 11; ** p < 0.01). (C) PEG-900 permeabilities for TRa-8 and also TRa-4 cells were reduced (n = 4 and 6; * p < 0.05; and n = 7; ** p < 0.01, respectively). (D) Permeability for FITC-dextran 4 kDa (FD4) was strongly decreased already in TRa-4 cells and also in TRa-8 cells (n = 6 and 6; ** p < 0.01; and n = 8; *** p < 0.001). (E) Permeability for FITC-dextran 10 kDa (FD10) showed a pattern similar to that of FD4, with even lower values in TRa-8 cells (n = 5 each; ** p < 0.01). (F) Permeability for FD20 (10^{-9} cm/s) in control cells was 20 times lower than that for FD10 and was not significantly altered in both tricellulin-transfected clones (n = 6, 5, and 6). (G) Permeability for the transcytotic marker HRP. Permeabilities for HRP (10^{-12} cm/s) remained the same in mock- and both tricellulin-transfected clones, indicating that the rate of transcytosis is not changed because of TRIC-a overexpression (n = 4, 5, and 4). (H) An unchanged percentage of TUNEL-positive cells revealed no changes in apoptosis because of overexpression of TRIC-a (n = 6).

17 nm; TRa-4, 277 ± 25 nm; TRa-8, 298 ± 25 nm; Figure 10C). The number of breaks (>20 nm) per μm horizontal length of single-strands in bTJ was not significantly different between controls and TRa-4, but clearly was reduced in TRa-8 (control, 1.60 ± 0.15; TRa-4, 1.40 ± 0.09; TRa-8, 0.40 ± 0.10,

*** p < 0.001, Figure 10D). In no case were breaks cumulated in a vertical series that could open a complete paracellular path. More importantly, analysis of strand appearance as being either of continuous type or particle (pearl string) type revealed changes that correlated with the observations re-
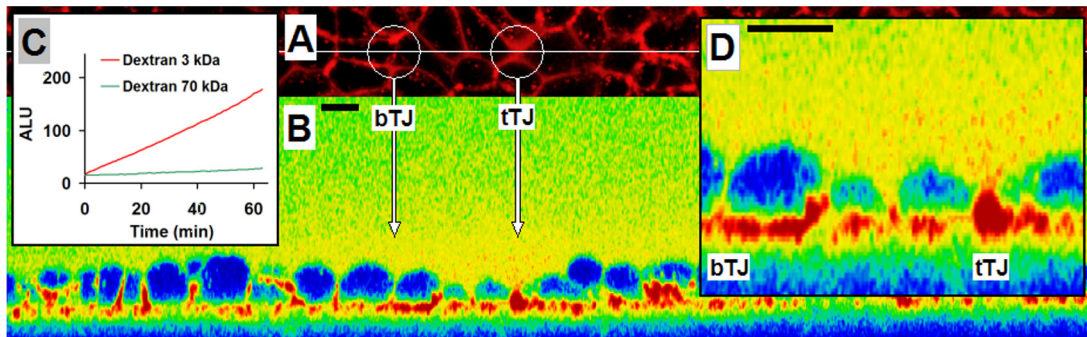
Figure 8. Fluorescence live-cell imaging of molecule passage. Bars, 10 μm. (A) XY image of a control monolayer basally perfused with TMR-dextran 3 (red) and OG-dextran 70 (green). The white line marks the position of XZ line scans. (B) Line scan image of 3-kDa dextran at 23 min after dextran addition. Arrows indicate corresponding structures (bTJ and tTJ), and the 3-kDa dextran is visualized. (C) Comparison of signal intensity (as arbitrary light units or ALU) over time for 3- and 70-kDa dextrans. As a region of interest (ROI), an area above the monolayer was chosen. The 3-kDa dextran passes the cell monolayer, whereas the signal for the not passing 70-kDa dextran remains constant over time. (D) Magnified detail of line-scan image. A 3-kDa dextran passage is already detectable 23 min after addition at tTJs, whereas in bTJ signals are still low.

ported above. Continuous strands appeared only in approximately half of the examined microscopy fields in controls as well as in TRa-4, whereas they predominated in TRa-8 (controls, 57% continuous; TRa-4, 52% continuous; TRa-8,100% continuous, Figure 10E). The predominant appearance of continuous strands as seen in TRa-8 was confirmed by analysis of a second bTJ clone, TRa-12 (Supplemental Material 3; Figure 4). Thus, the reduced number in TJ strand breaks and the transition from particle-type to continuous strands indicates that overexpression of TRIC-a in bTJ alters bTJ ultrastructure toward enhanced structural integrity.

Tricellular Junctions Are Not Altered Ultrastructurally by Tricellulin Overexpression

Compared with vector controls, in both overexpression clones no ultrastructural change was detectable when additional TRIC-a was incorporated into the tTJ. The tTJs of both TRIC-a overexpression clones did not differ in any of the analyzed parameters and therefore were combined into one group, tTJ TRa-4/-8 (Figure 9, D–F). The number of horizontal strands in tTJs of controls and both clones was nearly four times higher than in bTJs (*** p < 0.001, Figure 10B),

along with a 3.5 times larger meshwork depth in tTJs (*** p < 0.001, Figure 10C). Calculating the strand density as the ratio of strand number (Figure 10B) over meshwork depth (Figure 10C), it was found to be constant in all bTJ and tTJ groups. Notably, breaks per μm length of horizontal strands and continuous type strands of all tTJ groups resembled those seen in bTJ of TRa-8 cells, where TRIC-a was highly overexpressed (Figure 10, D and E). Finally, the length of the central tube of all tTJs was 1025 ± 135 nm (n = 13). This value matches closely with the length of 1 μm reported for jejunal epithelium (Staehelin, 1973).

DISCUSSION

Regionally Distinct Overexpression Allowed Mechanistic Characterization of Tricellulin

The ultrastructure of tTJs has been described almost four decades ago as vertical extensions of three joining bicellular TJs forming a central sealing element with a central tube (Staehelin *et al.*, 1969; Wade and Karnovsky, 1974). Although direct measurements were lacking, tTJs were predicted to be
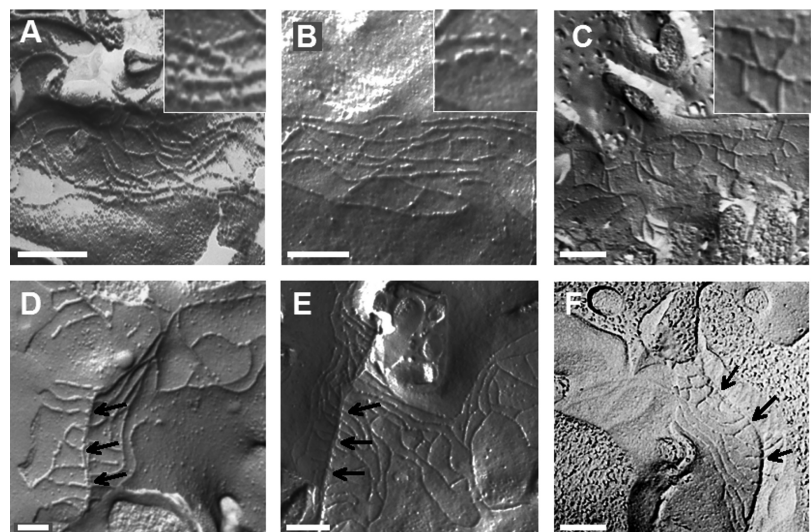
Figure 9. Freeze-fracture electron microscopy. Bars, 200 nm. Arrows indicate the central tube in images D–F. (A) bTJ strands of the vector-transfected cells revealed a regular meshwork, characterized by particle-type and continuous areas, as it is well visible in the magnified detail. (B) bTJs of TRa-4 cells show no ultrastructural difference compared with the mock-transfected cells and also have particle-type strands. (C) A remarkable difference from the vector-transfected and TRa-4 cells is the complete absence of particle-type strands in bTJs of TRa-8 cells. (D) The tTJs of vector-transfected cells are characterized by linear, continuous strands expanding vertically. (E) There is no obvious difference in tTJs of TRa-4 and the vector-transfected cells. The linear orientations of TJ strands form a fishbone-like structure. (F) The tTJs of TRa-8 cells showed no difference to mock-transfected or TRa-4 cells.
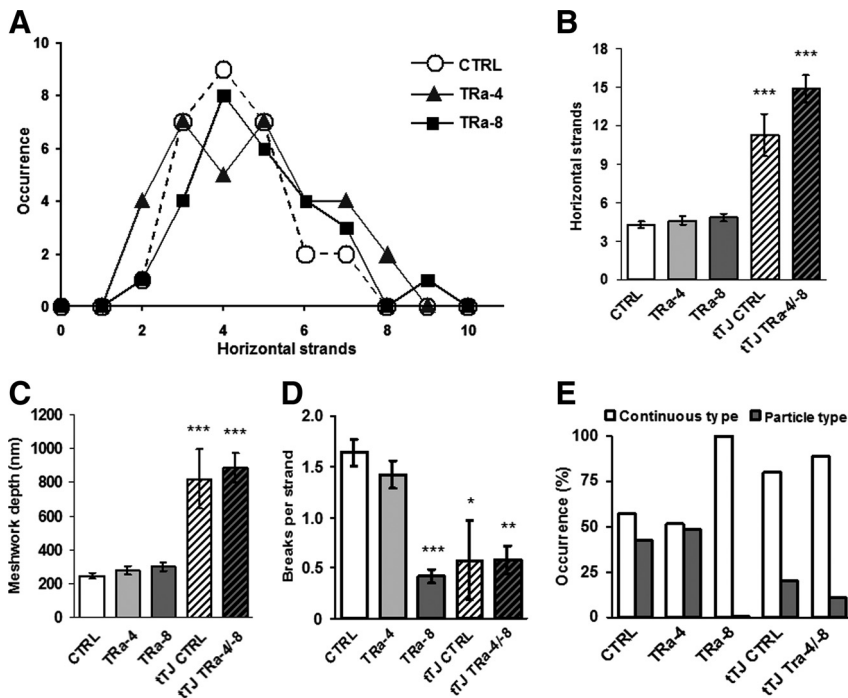
Figure 10. Morphometric analysis of TJ ultrastructure. (A) Transfection with TRIC-a did not alter the occurrence of strand numbers. (B) In bTJs there was no difference between the vector-transfected, TRa-4, and the bicellular overexpressing TRa-8 cells. In contrast, tTJs of both, controls and TRa-4 and TRa-8 cells (taken together to TRa-4/-8) revealed nearly four times more TJ strands (n = 11, 11, 10, 4, and 9; *** p < 0.001). (C) The vertical depth of the compact meshwork did not change after insertion of additional TRIC-a. tTJs in comparison had an expanded meshwork (*** p < 0.001) (D) Occurrence of breaks >20 nm/μm length of single horizontal strands. Bicellular overexpression of TRIC-a (TRa-8) led to about threefold reduction of breaks, close to that found in tTJs (*** p < 0.001). (E) Occurrence of continuous and particle strand type. Bicellular overexpression of TRIC-a (TRa-8) led to complete disappearance of particle-type horizontal strands in bTJs, again close to that found in tTJs.

weak, highly permeable regions of the paracellular barrier (Wade and Karnovsky, 1974; Walker *et al.*, 1994). It was not until 2005, however, that a protein, that is preferentially located at tTJ, was discovered (Ikenouchi *et al.*, 2005) and accordingly named tricellulin. To date, four human tricellular isoforms have been described (Riazuddin *et al.*, 2006). Mutations of TRIC-a, the longest human isoform, have been reported to result in a human hereditary disease, nonsyndromic deafness (DFNB49), indicating that TRIC-a is crucial for keeping up a strong K^+ potential that occurs in the inner ear (Riazuddin *et al.*, 2006).

In pioneer studies of Shoichiro Tsukita suppression of TRIC-a led to compromised barrier function and disorganized tricellular and bicellular TJs (Ikenouchi *et al.*, 2005). However, local barrier functions of TRIC-a were not known yet. Contrary to the above approach, we overexpressed TRIC-a in a cell line with low endogenous tricellulin expression and chose two different clones for a detailed analysis of bTJ and tTJ barrier mechanisms. In clone TRa-4, TRIC-a was predominantly localized in tTJs and moderately overexpressed, comparable to the endogenous expression levels of the human intestinal cell lines CaCco-2 and HT-29/B6. Being well-established models for human colonic epithelia, the expression profile of those cell lines could be taken as an estimate for tricellulin levels existing in the human colon. Thus, the vector-transfected controls, exhibiting low tricellulin expression, may be taken as an intestinal model for slightly down-regulated tricellulin, whereas clone TRa-4 may reflect the conditions of a human tissue like colonic epithelium.

In the second clone, TRa-8, which had fourfold higher expression than clone TRa-4, the additional TRIC-a was localized in bTJs. Therefore, this clone was used to describe effects on the bTJ.

Overexpression of TRIC-a did not change the overall molecular composition of the TJ as judged by the lack of changes in the expression of occludin and claudin-1 to -4. Changes in claudin-2 expression in TRa-4 cells were shown

to be without functional relevance because of extrajunctional localization.

Tricellulin Reduces bTJ Ion Permeability without Change in Selectivity or Charge Preference

A distinct increase in transepithelial resistance was detected only in clone TRa-8 that presented bicellular and tricellular TRIC-a localization, whereas pure tricellular overexpression in clone TRa-4 showed no measurable effect. Differentiation into trans- and paracellular resistance by two-path impedance spectroscopy revealed that this increase originated in a greatly elevated paracellular resistance without significant effect on cell membrane resistance.

Dilution potential measurements yielded no differences in the ratio of cation over anion permeability in controls and both clones. Therefore, TRIC-a overexpression tightens the barrier for ions without charge preference.

In solution, ions are surrounded by a hydration shell, which is formed by water molecules of an orientation depending on the ion's charge. Eisenman and Sherry sequences allow to characterize ion binding sites within the TJ pore with respect to their electrostatic interaction, which can be interpreted as different degrees of hydration shell removal (Eisenman, 1962; Diamond and Wright, 1969). Bicellular overexpression of TRIC-a resulted in decreased permeabilities to all ions tested, but only minor shifts of Eisenman and Sherry sequences, indicating that TRIC-a does not substantially alter paracellular selectivity for ions.

As to the question of how tricellulin implements sealing against ions and larger solutes, several mechanisms can be ruled out: Other claudins were not altered in a way that can explain the action of tricellulin. Especially a change of claudins with known ion or charge selectivity like the cation channel-former claudin-2 can be excluded because there was no effect on ion or charge selectivity. Also, in other tested clones there was no change in charge selectivity (Supplemental Material 3; Figure 2B). Transcytosis and apoptosis were not altered by tricellulin overexpression. What remains

are the mechanistic implications of ultrastructural changes of the bTJ.

In bTJs Tricellulin Reduces Strand Discontinuities and by This Permeability

In RNAi experiments a critical loss of tricellulin had a weakening effect on TJ ultrastructure and may have finally led to a disruption of the junctional complex (Ikenouchi et al., 2005). In our TRIC-a overexpression experiments the opposite occurred in bTJs: Although the meshwork depth and the strand number remained constant in comparison to controls, the occurrence of breaks >20 nm was decreased, and strand type changed to 100% continuous. A similar correlation between strand linearity and paracellular resistance was found in human colon to be induced by a strong upregulation of claudin-2 in Crohn's disease (Zeissig et al., 2007). It is established that, depending on the presence of claudin-2, strand discontinuities appear or disappear (Furuse et al., 1999). In our study, discontinuities disappear although claudin-2 is not reduced, apparently caused by TRIC-a overexpression.

Breaks per se, as rare as found here, may not play a significant role for permeability. They occasionally reduced the number of barrier-forming meshwork loops by one (e.g., from four to three) but in no case opened a complete vertical path. In contrast, the TRIC-a–induced change toward continuous-type strands affects the entire meshwork and thus may indeed be related to the observed decrease in permeabilities. It is unclear yet, whether strand linearity is a direct determinant of permeability or if it represents an epiphenomenon of an altered composition of proteins within the TJ. Although homophilic interaction of single claudins has started to be understood (Yu et al., 2009; Piontek et al., 2008), the molecular base of strand formation of an ensemble of TJ proteins has not been experimentally addressed.

Thus, we conclude cautiously that the tricellulin-induced increase in linearity of bTJ strands is associated with the decreased permeability to ions and larger solutes.

tTJ Central Tubes Contribute ~1% to Overall Conductance

The finding that in tricellular junctions after overexpression of TRIC-a (clone TRa-4) the permeability for 4- and 10-kDa macromolecules was reduced to one fifth or less, whereas that for ions and midsize solutes was not significantly altered (Figure 7, D and E, vs. 5A), which seems to be contradictory.

However, we can readily explain this paradox by the rareness and the dimensions of tTJs compared with bTJs. From fluorescence-labeled MDCK II cells, morphometric parameters were estimated using Image J (http://rsb.info.nih.gov/ij/) with the MBF particle analysis plugin, which resulted in an average cell surface area of 100 μm^2 and a cell density of 10^6 cells/cm^2. The total length of the bTJ was found to be 20.6 m/cm^2. However, the TJ length per cell was 41 μm, because two cells share one bTJ. The average number of tTJs was 1.6×10^6 tTJs/cm^2 leading to 4.8 tricellular contacts per cell, because each tTJs is shared by three cells.

One of two estimations for the tricellular conductance was based on an upper limit calculation, where it was assumed that ions within the tricellular pore move as in free solution, The bath solution of the Ussing chamber has a specific conductance of 18.6 mS/cm (=mS·cm/cm^2). For one central tube of the given dimensions, this would be equivalent to a single-pore conductance of 146 pS. The second estimation for a lower limit of conductance used data for the claudin-2 pore, as a highly selective and narrow pore. This pore has been modeled to be 3.2 nm in length and 0.75 nm in diameter, and its conductance was estimated to be 70–100 pS by calculations depending on Brownian Dynamics simulations (Yu et al., 2009). Assuming that the tricellular central tube (Staehelin, 1973) behaved as if it was constructed from units with the dimensions and characteristics of claudin-2 pores, we calculated the equivalent number of claudin-2 pore units to be 178 in parallel, $\times$ 313 in series. Using these numbers, a conductance for one tricellular central tube of ~40–60 pS was calculated (more information in Supplemental Material 2).

Referring to the pore density, the contribution of tricellular central tubes to total conductance of a MDCK II cell layer is thus between 60 and 240 $\mu S/cm^2$. The paracellular conductance of MDCK II cell layers amounted to 23 mS/cm^2 (data from Figure 4), was leading to a contribution of tricellular central tubes toward this paracellular conductance of 1%.

Thus, if TRIC-a overexpression reduced this value even to zero, this would not notably affect total paracellular conductance. It was therefore no surprise that with our conductance scanning technique (Gitter et al., 1997; Yu et al., 2009) we did not detect elevated local conductances at tTJs (data not shown). This aspect is in accordance with results published by Cereijido et al. (1982) for the Necturus gallbladder. In conclusion, TRIC-a overexpression in tTJs does not alter overall ion permeability, because the contribution of tTJs is negligible compared with that provided by the bTJs and the cell membranes.

From Size Estimations It Is Comprehensible That Macromolecules Pass across the tTJ Central Tube

The conductance of the tTJ central tube of 146 pS is comparable to that of the largest membrane channels, e.g., maxi-K^+ channels, which, however, do not allow macromolecular permeation. To explain this aspect of the paradox, one has to take into account that the central tube is much wider but also far longer than any membrane channel. Comparing the Stokes radius of 10-kDa dextran (2.3 nm) with the minimally assumed radius of the central tube (5 nm; Staehelin, 1973) it is conceivable that 10-kDa dextran may easily permeate along the tTJ central tube and, within this tube, is probably not much more restricted in movement than monovalent ions.

Under the precaution that dimensions of the tTJ central tube are known only roughly, we suggest that macromolecules cross epithelial layers primarily along the central tube of tTJs. The mechanism by which TRIC-a alters tTJ permeability without visibly changing its ultrastructure must be left open presently. The existence of narrow spots within the tTJ central tube has been postulated earlier (Staehelin, 1973). Considering this, it is tempting to speculate that TRIC-a inserts into the tTJ in a way that reduces the diameter of the central tube to a size critical for macromolecule passage.

To directly demonstrate macromolecule permeation across the TJ we developed a fluorescence live-cell imaging technique of molecular passage and were able to visualize the passage of 3-kDa dextran across paracellular sites of control cells. Though close to the present limit of resolution of our method, molecular passage could be demonstrated at tTJs but was also present at bTJs. Also from these findings it is comprehensible that a major site of macromolecule permeation in MDCK II monolayers is indeed the tTJ.

A Model Consisting of Frequent Small Permeation Sites and Rare Large Pores

The paracellular barrier to uncharged solutes in MDCK II cells has been modeled as two distinct and independent pathways (Watson *et al.*, 2001; Van Itallie *et al.*, 2008), high-capacity "small pores" with a radius of 0.4 nm and a size-independent pathway allowing the flux of larger solutes. The permeability to small solutes was suggested to be proportional to the pore number and the profile of TJ proteins expressed.

Our present findings are widely consistent with this model, and we would assign the two pathways to distinct locations of the TJ: The high-capacity "small pores" are integral part of the bicellular junctions and are frequent enough to carry ~99% of the paracellular permeability for ions. The permeability of these small pores for larger molecules is limited to a dextran size below 20 kDa.

For the size-independent "large pore," in contrast, we suggest that its physical basis is represented by the tricellular central tube. It is wide enough to generally allow the passage of large solutes, but so rare that it may only contribute to ~1% of the paracellular ion permeability. TRIC-a expression above endogenous levels tightens both pathways in a specific way depending on its localization in bTJs or tTJs.

ACKNOWLEDGMENTS

REFERENCES

Amasheh, S., Meiri, N., Gitter, A. H., Schöneberg, T., Mankertz, J., Schulzke, J. D., and Fromm, M. (2002). Claudin-2 expression induces cation-selective channels in tight junctions of epithelial cells. J. Cell Sci. *115*, 4969–4976.

Cereijido, M., Stefani, E., and Chavez de Ramirez, B. (1982). Occluding junctions of the *Necturus* gallbladder J. Membr. Biol. *70*, 15–25.

Chishti, M. S., Bhatti, A., Tamim, S., Lee, K., McDonald, M. L., Leal, S. M., and Ahmad, W. (2008). Splice-site mutations in the TRIC gene underlie autosomal recessive nonsyndromic hearing impairment in Pakistani families. J. Hum. Genet. *53*, 101–105.

Diamond, J. M., and Wright, E. M. (1969). Biological membranes: the physical basis of ion and nonelectrolyte selectivity. Annu. Rev. Physiol. *31*, 581–656.

Eisenman, G. (1962). Cation selective glass electrodes and their mode of operation. Biophys. J. *2*, 259–323.

Florian, P., Amasheh, S., Lessidrensky, M., Todt, I., Bloedow, A., Ernst, A., Fromm, M., and Gitter, A. H. (2003). Claudins in the tight junctions of stria vascularis marginal cells. Biochem. Biophys. Res. Commun. *304*, 5–10.

Furuse, M., Hirase, T., Itoh, M., Nagafuchi, A., Yonemura, S., Tsukita, S., and Tsukita, S. (1993). Occludin: a novel integral membrane protein localizing at tight junctions. J. Cell Biol. *123*, 1777–1788.

Furuse, M., Fujita, K., Hiiragi, T., Fujimoto, K., and Tsukita, S. (1998). Claudin-1 and -2, novel integral membrane proteins localizing at tight junctions with no sequence similarity to occludin. J. Cell Biol. *141*, 1539–1550.

Furuse, M., Sasaki, H., and Tsukita, S. (1999). Manner of interaction of heterogeneous claudin species within and between tight junction strands. J. Cell Biol. *147*, 891–903.

Furuse, M., Furuse, K., Sasaki, H., and Tsukita, S. (2001). Conversion of zonulae occludentes from tight to leaky strand type by introducing claudin-2 into Madin-Darby canine kidney I cells. J. Cell Biol. *153*, 236–272.

Gitter, A. H., Bertog, M., Schulzke, J. D., and Fromm, M. (1997). Measurement of paracellular epithelial conductivity by conductance scanning. Pfluegers Arch. *434*, 830–840.

Günzel, D., Stuiver, M., Kausalya, P. J., Haisch, L., Rosenthal, R., Krug, S. M., Meij, I. C., Hunziker, W., Fromm, M., and Müller, D. (2009). Claudin-10 exists in six alternatively spliced isoforms which exhibit distinct localization and function. J. Cell Sci. *122*, 1507–1517.

Ikenouchi, J., Furuse, M., Furuse, K., Sasaki, H., Tsukita, S., and Tsukita, S. (2005). Tricellulin constitutes a novel barrier at tricellular contacts of epithelial cells. J. Cell Biol. *171*, 939–945.

Ikenouchi, J., Sasaki, H., Tsukita, S., Furuse, M., and Tsukita, S. (2008). Loss of occludin affects tricellular localization of tricellulin. Mol. Biol. Cell *19*, 4687–4693.

Kreusel, K. M., Fromm, M., Schulzke, J. D., and Hegel, U. (1991). Cl⁻ secretion in epithelial monolayers of mucus-forming human colon cells (HT-29/B6). Am. J. Physiol. *261*, C574–C582.

Piontek, J., Winkler, L., Wolburg, H., Müller, S. L., Zuleger, N., Piehl, C., Wiesner, B., Krause, G., and Blasig, I. E. (2008). Formation of tight junction: determinants of homophilic interaction between classic claudins. FASEB J. *22*, 146–158.

Reiter, B., Kraft, R., Günzel, D., Zeissig, S., Schulzke, J. D., Fromm, M., and Harteneck, C. (2006). TRPV4-mediated regulation of epithelial permeability. FASEB J. *20*, 1802–1812.

Riazuddin, S., *et al.* (2006). Tricellulin: a novel tight junction protein necessary for hearing. Am. J. Hum. Genet. *79*, 1040–1051.

Schlüter, H., Moll, I., Wolburg, H., and Franke, W. W. (2007). The different structures containing tight junction proteins in epidermal and other stratified epithelial cells, including squamous cell metaplasia. Eur. J. Cell Biol. *86*, 645–655.

Schneeberger, E. E., and Lynch, R. D. (2004). The tight junction: a multifunctional complex. Am. J. Physiol. Cell Physiol. *286*, C1213–C1228.

Staehelin, L. A., Mukherjee, T. M., and Williams, A. W. (1969). Freeze-etch appearance of tight junctions in the epithelium of small and large intestine of mice. Protoplasma *67*, 165–184.

Staehelin, L. A. (1973). Further observations of the fine structure of freeze-cleaved tight junctions. J. Cell Sci. *13*, 763–786.

Stevenson, B. R., Anderson, J. M., Goodenough, D. A., and Mooseker, M. S. (1988). Tight junction structure and ZO-1 content are identical in two strains of Madin-Darby canine kidney cells which differ in transepithelial resistance. J. Cell Biol. *107*, 2401–2408.

Tsukita, S., Furuse, M., and Itoh, M. (2001). Multifunctional strands in tight junctions. Nat. Rev. Mol. Cell Biol. *2*, 285–293.

Van Itallie, C. M., and Anderson, J. M. (2004). The molecular physiology of tight junction pores. Physiology *19*, 331–338.

Van Itallie, C. M., Holmes, J., Bridges, A., Gookin, J. L., Coccaro, M. R., Proctor, W., Colegio, O. R., and Anderson, J. M. (2008). The density of small tight junction pores varies among cell types and is increased by expression of claudin-2. J. Cell Sci. *121*, 298–305.

Wade, J. B., and Karnovsky, M. J. (1974). The structure of the zonula occludens. A single fibril model based on freeze-fracture. J. Cell Biol. *60*, 168–180.

Walker, D. C., MacKenzie, A., and Hosford, S. (1994). The structure of the tricellular region of endothelial tight junctions of pulmonary capillaries analyzed by freeze fracture. Microvasc. Res. *48*, 259–281.

Walker, D. C., MacKenzie, A., Hulbert, W. C., and Hogg, J. C. (1985). A re-assessment of the tricellular region of epithelial cell tight junctions in trachea of guinea pig. Acta Anat. *122*, 35–38.

Watson, C. J., Rowland, M., and Warhurst, G. (2001). Functional modeling of tight junctions in intestinal cell monolayers using polyethylene glycol oligomers. Am. J. Physiol. Cell Physiol. *281*, C388–C397.

Yu, A.S.L., Cheng, M. H., Angelow, S., Günzel, D., Kanzawa, S. A., Schneeberger, E. E., Fromm, M., and Coalson, R. D. (2009). Molecular basis for cation selectivity in claudin-2-based paracellular pores: Identification of an electrostatic interaction site. J. Gen. Physiol. *133*, 111–127.

Zeissig, S., Bürgel, N., Günzel, D., Richter, J. F., Mankertz, J., Wahnschaffe, U., Kroesen, A. J., Zeitz, M., Fromm, M., and Schulzke, J. D. (2007). Changes in expression and distribution of claudin-2, -5 and -8 lead to discontinuous tight junctions and barrier dysfunction in active Crohn's disease. Gut *56*, 61–72.